Lightweight Human-Friendly Robotic Arm Based on Transparent Hydrostatic Transmissions

Marco Bolignari [ORCID], Gianluca Rizzello [ORCID], *Member, IEEE*, Luca Zaccarian [ORCID], *Fellow, IEEE*, and Marco Fontana [ORCID], *Member, IEEE*

Abstract—We present theoretical and experimental results regarding the development and the control of a two-link robotic arm with remotized actuation via rolling diaphragm hydrostatic transmissions. We propose a dynamical model capturing the essential dynamics of the developed transmission/robot ensemble and implement a control strategy consisting of two nested loops, the inner one performing high-bandwidth joint torque regulation and the outer one producing various types of compliance responses for effective human–robot interactions. Extensive sets of experiments, testing both the low-level torque controller and the high-level compliance controller, confirm the effectiveness of the proposed hardware-software remotization architecture.

Index Terms—Compliance and impedance control, force control, mechanism design, tendon/wire mechanism.

I. INTRODUCTION

A. Background

MODERN robots are progressively spreading in anthropic domains, and several activities of human life are increasingly being supported by robotic devices that closely interact with humans. In particular, direct physical human–robot interaction (pHRI) [1] is intrinsically required in several applications, including assistive/collaborative robots, rehabilitation exoskeletons, haptics/teleoperation robots among others. The design of robots for pHRI is driven by safety and dependability requirements, however, suitable levels of performance must also be guaranteed in terms of speed, power, bandwidth, and accuracy in position and force control. Conventional robots are intrinsically unsafe due to their high-mechanical impedance, but can be partially made safe through lightweight structural design, sensing, and closed-loop active impedance controllers, which improve their force control quality [2]. However, this comes at the cost of imposing limitations on performance in terms of speed and frequency bandwidth, because stability issues and velocity constraints place upper bounds on the admissible values of the control gains. In addition, the limited bandwidth also compromises safety, as the force exchanged between the robot and the humans can not be modulated in the event of accidental collisions, which are exactly characterized by high-frequency dynamics.

To effectively overcome these limitations, novel hardware design paradigms have been proposed, where the demanded safety and performance features are directly embedded within the intrinsic open-loop response of suitably conceived smart mechanical architectures. As an example, series elastic actuators (SEA) achieve safety over a broad range of frequencies by employing compliant drivetrains to dynamically decouple the actuators and link inertias [3]. However, the drivetrain elasticity inherently limits their control bandwidth. Variable stiffness actuators (VSA) [4] overcome this drawback, by modulating the drivetrain stiffness in order to tailor safety and performance properties according to instantaneous needs. Nevertheless, hardware solutions for stiffness modulation increase the robot complexity, the encumbrance, and the mass, possibly jeopardizing most of their theoretical advantages.

An effective solution to address the safety/performance tradeoff is offered by remotization strategies, where the actuators are placed far from the robot joints, e.g., at the robot base, and power transmission systems are used to transfer the torques from the actuators to the actuated joints. This provides two main advantages: 1) the motors are stationary, thus, highly reducing the mass of the moving links; 2) the actuators' mass is not a parameter to be minimized any longer, thus, direct-drive (or quasi-direct-drive) actuators, which exhibit low inertia, can be employed. This reduction in moving masses and inertia results in low kinetic energy of the system even during high-speed movements, intrinsically minimizing injury hazard with accidental collisions. Additionally, low-inertia designs, in conjunction with

Marco Bolignari is with the Institute of Mechanical Intelligence and Department of Excellence of Robotics and AI, Scuola Superiore Sant'Anna, 56100 Pisa, Italy, and also with the Department of Industrial Engineering, University of Trento, 38123 Trento, Italy (e-mail: marco.bolignari@santannapisa.it).

Gianluca Rizzello is with the Department of Systems Engineering, Saarland University, DE 66123 Saarbrücken, Germany (e-mail: gianluca.rizzello@ imsl.uni-saarland.de).

Luca Zaccarian is with the Laboratory for Analysis and Architecture of Systems, Université de Toulouse, CNRS, 31400 Toulouse, France, and also with the Department of Industrial Engineering, University of Trento, 38123 Trento, Italy (e-mail: luca.zaccarian@unitn.it).

Marco Fontana is with the Institute of Mechanical Intelligence and Department of Excellence of Robotics and AI, Scuola Superiore Sant'Anna, 56100 Pisa, Italy (e-mail: marco.fontana@santannapisa.it).

This article has supplementary material provided by the authors and color versions of one or more figures available at https://doi.org/10.1109/TRO.2023.3290310.

Digital Object Identifier 10.1109/TRO.2023.3290310

low-friction, high-stiffness transmissions, can enhance robot performance in terms of speed, acceleration, and bandwidth.

Steel-cable/pulley transmissions have been extensively studied and implemented as a means for remotization, because of their efficiency, lightweight, and reduced encumbrance [5], [6], [7], [8]. However, the structural complexity resulting from the cable routing is generally high and it largely increases with the number of degrees of freedom. Moreover, the need for deviating heavily loaded cables about a multitude of pulleys generally introduces compliance in the transmission, which limits the closed-loop torque-control bandwidth, and generates undesired nonlinear frictional effects in multi-DoF systems. The use of Bowden cables can be an alternative choice to reduce the system complexity and cost, but the mechanical transparency is penalized due to friction, wear, backlash, and low-bandwidth.

Recently, rolling diaphragm hydrostatic transmissions (RDHT) have been conceived as an attractive solution for the remotization of the actuators. RHDTs are special hydrostatic transmissions that use hydraulic cylinders based on rolling diaphragms, i.e., elastomeric parts that roll from the bore to the piston surfaces during motion, thus, preventing sliding friction, wear, and leakage problems [9]. RDHTs offer a combination of desirable features for designing human-friendly robotic arms, as they make it possible to achieve both low-impedance and high-bandwidth, by combining the low-inertia and ease in control of lightly geared electric motors with the high stiffness and high specific torque of hydraulic systems. Compared to traditional valve-driven hydraulic devices, RDHT-based systems show intrinsic backdrivability and low output impedance because the fluid pressure is directly modulated by the input torque generated by an electric motor, instead of controlling the flow rate by means of valves. Moreover, static friction is strongly reduced by using rolling-diaphragm cylinders and backlash can be prevented by pairing two hydrostatic lines in an antagonistic configuration [9]. Viscous friction can be easily compensated for, as it is conveniently independent of the transmitted torque and of the fluid pressure [10]. In addition, the indirect measurement of the transmitted torque by means of pressure sensors is an effective strategy to generate an accurate feedback signal for large-bandwidth torque control [11]. Finally, relaxed requirements on the manufacturing tolerances enable low-cost production. In less than a decade, this novel technology rapidly gained attractiveness and a variety of RDHT-based devices have been proposed. Examples are passive telepresence systems [12], robots for extending the reach inside MRI bores [13] and similar MRI compatible devices [14], [15], [16], upper-limb [17] and lower-limb [18], [19] exoskeletons, wearable supernumerary arms [20], [21] and legs [22], as well as robotic grippers [23] and agile legged robots [24].

B. Contributions

The use of hydrostatic transmissions in robotics is relatively novel and the research on advanced strategies to design RDHT robots for pHRI is still marginally addressed. In these regards, this work defines a renewed approach to the development of accurate and transparent RDHT robots for pHRI. Based on the synergy between novel hardware and control design, we devise a pressure-based closed-loop interaction control scheme applied to a novel high-efficiency RDHT robot actuated by direct-drive electric motors.

Only small-scale devices have been developed in the direction of coupling direct drive motors and hydrostatic transmissions, such as force-controllable grippers [23], which exploit pressure sensing to reduce the hysteresis and extend the frequency-response bandwidth [25]. However, results obtained with small-scale systems are hardly useful when designing multi-DoF humanlike robotic arms due to important dynamical effects emerging in large-scale systems. Preliminary assessments of force-controllable larger-scale robots have only been studied for portable and wearable applications [20]. The obtained results are quite promising in terms of force bandwidth, which exceeds 10 Hz, and robot mass (excluded the actuation unit), which is lower than the admissible payload. However, its peculiar actuation design, based on a combination of magnetorheological (MR) clutches and ball screws, penalizes the efficiency (especially when the system is idling or delivering small forces) and the backdrivability, as the friction increases as a function of the transmitted torque [20]. Preliminary compensation strategies have been proposed in [26] for a single DoF. More advanced control approaches for RHDTs have been studied on a 1-DoF testbench by the authors of this manuscript in [11], introducing a Smith-predictor-based torque control relying on pressure feedback.

This work presents a novel 2-DoF RDHT-based robotic arm for high-quality pHRI. A simple and reliable hardware design is pursued, where direct drive electric motors provide low output inertia, while highly efficient hydrostatic transmissions, based on floating cylinders [10], ensure enhanced transparency and backdrivability. We propose concurrently a novel approach to force-control of RDHTs; as compared to [11], we abandon the need of a Smith-predictor solution, thanks to hardware improvements, and we address the more challenging nonlinear problem associated to a multi-DoF dynamics, which we validate by experiments performed on our novel prototype. We analyze the open-loop force-controlled response of the robot and we model the essential dynamical structure of hydrostatic robotic arms. We then introduce a novel hierarchical closed-loop force control architecture ensuring regulation of the mechanical interaction at the robot end-effector. Our solution is based on a high-bandwidth low-level torque controller solely based on pressure sensing feedback, ensuring tight regulation of the torque transmitted to each robot joint. The low-level torque controllers are nested within a high-level human–robot interaction controller whose goal is the regulation of the overall robot interaction (i.e., active stiffness and damping) in the operational space. A comprehensive set of experiments well illustrates both the open-loop and the closed-loop response of RDHTs under several different pHRI situations, such as heavy load collaborative tasks, low or high frequency tests and virtual viscous/elastic resistance rendering tests. In addition to achieving efficiency and excellent controllability across a broad range of frequencies, the experiments

TABLE I
OVERVIEW OF THE MAIN VARIABLES USED IN THE ARTICLE

Notation
- Subscript j specifies the joint under consideration, e.g., θ_{r1} and θ_{r2}. ($j = 1$ "shoulder," $j = 2$ "elbow")
- Variables identifying the same quantity at different joints are often collected in vectors. Subscript j drops in this case, e.g., $\theta_r = [\theta_{r1}, \theta_{r2}]^\top$.
- Bold letters indicate variables in the Laplace domain without specifying explicitly variable "s", e.g., $\boldsymbol{\theta_{r1}} := \mathcal{L}[\theta_{r1}(t)]$.

Variable	Description	Vector
T_{rj}	Torque transmitted at the jth robot joint	$T_r = [T_{r1}, T_{r2}]^\top$
T_{mj}	Torque generated by the jth motor	$T_m = [T_{m1}, T_{m2}]^\top$
θ_{rj}	Angle of the jth robot joint	$\theta_r = [\theta_{r1}, \theta_{r2}]^\top$
θ_{mj}	Angle of the jth motor	$\theta_m = [\theta_{m1}, \theta_{m2}]^\top$
F_x, F_y	End-effector force in the workspace	$F = [F_x, F_y]^\top$
P_{ex}, P_{ey}	End-effector position in the workspace	$P_e = [P_{ex}, P_{ey}]^\top$
p_{Aj}, p_{Bj}	Pressure of transmission channels A and B	
m_{rj}	Link mass	
J_{rj}	Link inertia	
J_{mj}	Motor inertia	
k_{mj}	Transmission stiffness	
T_{cj}	Cogging-torque compensation term	$T_c = [T_{c1}, T_{c2}]^\top$
T_{fj}	Friction and spring-rate compensation term	$T_f = [T_{f1}, T_{f2}]^\top$
T_{aj}	Open-loop commanded torque at jth joint	$T_a = [T_{a1}, T_{a2}]^\top$
T_{sj}	Closed-loop torque setpoint at jth joint	$T_s = [T_{s1}, T_{s2}]^\top$

*The variables highlighted in light grey are control signals.

demonstrate that the proposed RDHT approach outperforms existing methods [20] in terms of actively controlled backdriveability, which is enhanced by almost an order of magnitude. This enhancement proves to be independent of the transmitted torque and displacement frequency. The same considerations apply to the force tracking performance, proving the proposed approach ideal for high-quality pHRI.

The rest of this article is organized as follows. Section II presents the design of the rolling diaphragm hydrostatic transmission and its integration in the robotic arm. Section III proposes and experimentally validates a general dynamical model describing the robot open-loop response; also, a low-level closed-loop torque controller based on pressure-measurement feedback is designed at each joint. In Section IV, the above-mentioned low-level control actions are nested within a high-level hierarchical controller regulating the overall human–robot interaction in the operational space. A comprehensive set of validation experiments is then conducted in Section V. Finally, Section VI concludes this article.

II. ROLLING DIAPHRAGM HYDROSTATIC TRANSMISSION LIGHTWEIGHT ARM

This chapter briefly introduces the working principle, Section II-A, and the technical specifications, Section II-C, of our lightweight arm. Section II-B describes the details of the remotely actuated robot joints. Table I offers an overview of the main variables used in the article and lists the taxonomy of the selected notation.

A. Arm Design and Operating Principle

Fig. 1(left) shows the lightweight robotic arm developed in this work. It consists of a 2-DOF planar manipulator, where low-friction rolling diaphragm hydrostatic transmissions are implemented to remotize the two electric motors, which are placed at the robot base. Each hydrostatic transmission connects the jth robotic joint ($j = 1$ referring to the "shoulder" joint, and $j = 2$ referring to the "elbow" joint) with the jth motor and comprises two fluid lines equally pressurized at the rest conditions, i.e., $p_{Aj} = p_{Bj} = p_0$. When a positive torque T_{mj} is generated by the jth motor, pressure p_{Aj} increases and pressure p_{Bj} decreases, thus, generating a differential pressure $\Delta p_j = p_{Aj} - p_{Bj}$ that propagates through the fluid lines up to the robotic joint, where two output cylinders convert it back into torque T_{rj}, Fig. 1(right), exerted on the joint axis. The same reasoning holds for negative torques, which generate a negative Δp_j instead. Notice that the prepressurization p_0 is set to one-half of the maximum operating differential pressure to enable bidirectional torque transmission and ensure that both $p_{Aj} > 0$ and $p_{Bj} > 0$. This is important in preventing diaphragm jamming [9]. Each hydrostatic transmission is symmetric, i.e., it implements equal input and output cylinders, and generates a unit transmission ratio. Under ideal or static conditions, we have $T_{rj} \approx T_{mj}$. This approximation, however, degrades when operating far from the static case due to viscous friction and structural dynamic effects, i.e., resonant modes, that become relevant at high operating frequencies. Improved accuracy is obtained here by sensing the transmitted torque T_{rj} by means of pressure sensors placed on the fluid lines close to the robot joint, see Fig. 1(right), and closing a low-level (joint-level) torque feedback loop.

A handle, placed at the end-effector, allows interacting with a human user during the experiments (see Section V). A load cell placed on the handle measures the interaction force $F = [F_x, F_y]^\top$ between the human operator and the robot. This sensor is only used here for validation purposes, without being involved in the force control feedback, which is solely based on pressure sensing.

B. Hydrostatic Robotic Joint

Fig. 1 (center) shows the proposed robotic joint and Fig. 1 (right) illustrates the pressure-to-torque transformation that takes place at the robot axes (the same transformation takes place at the input side, the transmission being symmetric). Two cylinders are coupled in an antagonistic configuration by two timing belts, which are routed around two output toothed pulleys. Each cylinder produces a linear force, proportional to its internal pressure and equivalent area A_e, on its corresponding belt branches

$$F_{Aj} = A_e p_{Aj}, \quad F_{Bj} = A_e p_{Bj}. \quad (1)$$

When pressures p_{Aj} and p_{Bj} coincide, the two cylinders are balanced and no torque is generated on the pulley. When the two pressures are different, instead, a net torque is expected at the joint, equal to

$$T_{rj} = r(F_{Aj} - F_{Bj}) = r A_e \Delta p_j \quad (2)$$

where constant r is the pulley radius. When filled with incompressible fluids, e.g., water, the transmissions achieve high stiffness and synchronous motion between the motor and joint rotations, i.e., $\theta_{rj} \approx \theta_{mj}$. In practice, some compliance exists along the hydraulic lines due to the presence of dissolved air
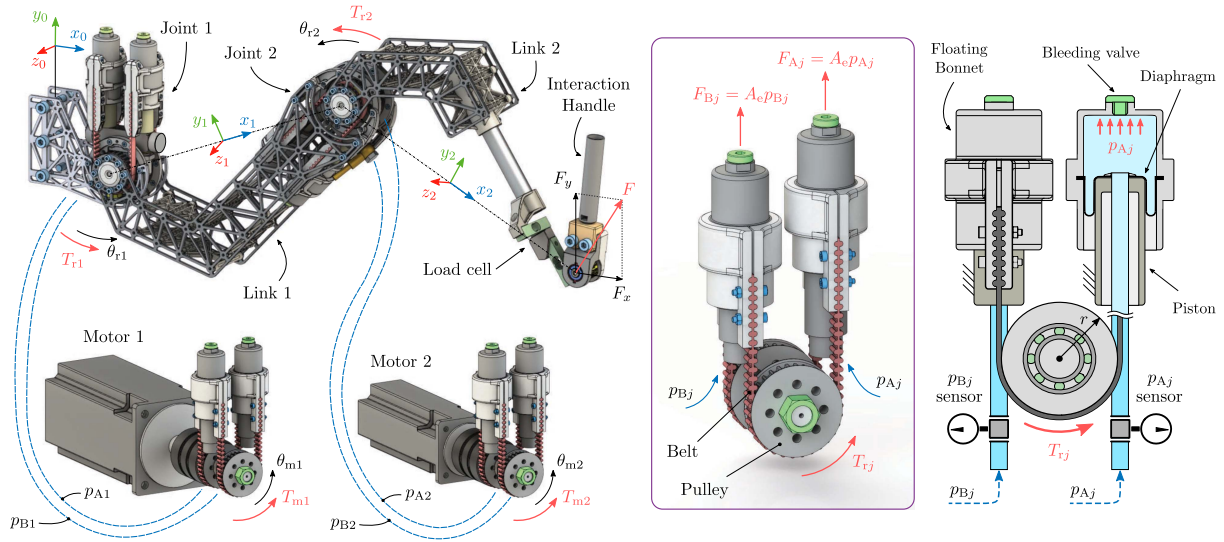
Fig. 1. Experimental prototype of the lightweight robotic arm. *Left:* Overall system; the blue dashed lines represent the hydraulic hoses. *Center:* Integrated robotic joint based on rolling diaphragm hydrostatic cylinders with floating-bonnet layout. *Right:* Schematic view of the joint architecture.

and the elasticity of the hoses, belts, and diaphragms. Therefore, this approximated kinematic relation among the two angles holds as long as the transmitted torque is reasonably small, and the operating frequency is significantly smaller than the first resonant mode.

Pistons, pressure sensors, and hydraulic hoses are assembled in a compact shape. Placing the pressure sensors in close proximity of the cylinder chambers is crucial for measuring joint torques $T_{\mathrm{r}j}$ through pressure sensing, exploiting (2), with high sensing bandwidth and accuracy. Sensing accuracy and mechanical transparency, peculiar to RDHTs in general, are here further enhanced using rolling diaphragm cylinders with floating-bonnet layout developed in [10], to completely prevent sliding and static friction.

C. Technical Specifications

The reach of the robotic arm is 640 mm, as the two links are 320 mm long. Its integrated joints, shown in Fig. 1 (center), have an angular range of $140°$, weigh 700 g (including two pressure sensors), and have been tested with torque loads up to 20 N·m. The integrated joint is conceived as a modular element, so that the same optimized design and dimensions are usable for all the robot joints. The cylinders are equipped with a *OA-106-145* rolling diaphragm from DiaCom Corp., characterized by an effective area $A_{\mathrm{e}} = 510$ mm^2, a 27 mm cylinder diameter, a 56.8 mm stroke, and a 25 bar maximum working pressure. Timing belts are routed around two output toothed pulleys, with primitive radius $r = 23.9$ mm. The joint angular position $\theta_{\mathrm{r}j}$ is measured by means of a RM08D01-12 magnetic incremental encoder from RLS (4096 cpr resolution), while the fluid pressures $p_{\mathrm{A}j}$ and $p_{\mathrm{B}j}$ are measured by means of two 3100x pressure sensors from Gems Sensors (16 bar maximum pressure measurement and 0.04 bar accuracy). The hydraulic hoses, characterized by a flexible coating of Kevlar

fibers, have a length of 1 m and an internal diameter of 5 mm; distilled water is used as working fluid. Two direct-drive motors AM8043 (4.90 N·m rated torque, 28.0 N·m peak torque) and AM8053 (14.9 N·m rated torque, 53.1 N·m peak torque) from Beckhoff are used for the actuation of elbow and shoulder joints, respectively. Both motors are equipped with a 24 bits (20 bits per revolution) multiturn absolute encoder, which measures the motor position $\theta_{\mathrm{m}j}$. The control unit consists of a CX51 Beckhoff Embedded-PC based on a TwinCAT real-time communication protocol. All of the experiments showed in this work were performed with a fixed sampling rate of 2 kHz.

III. MODELING AND LOW-LEVEL CONTROLLER

This section presents the dynamical model of the robotic system and its low-level controller, schematically represented in Fig. 2 (left) and Fig. 2 (right), respectively. Section III-A describes the precompensation of the disturbance effects caused by the torque ripple, static friction and viscous friction generated by the motors and the transmissions. Once these disturbances are compensated for, Section III-B presents the dynamical model of the precompensated robotic arm, and Section III-C deepens the analysis of the torque dynamics in the motor-transmission subsystems used to connect each motor to its corresponding robot joint. Finally, Section III-D describes the low-level closed-loop torque controller based on pressure-measurement feedback, used for tight regulation of the torque transmitted at each robot joint.

A. Cogging Torque, Friction, and Spring-Rate Compensation

Differently from the vast majority of robots, the mechanical transparency of the proposed architecture enables both open-loop (relying on the current-loop executed in the motor drivers) and closed-loop (relying on the pressure sensing of the transmission fluid) force control of the robot. Since the
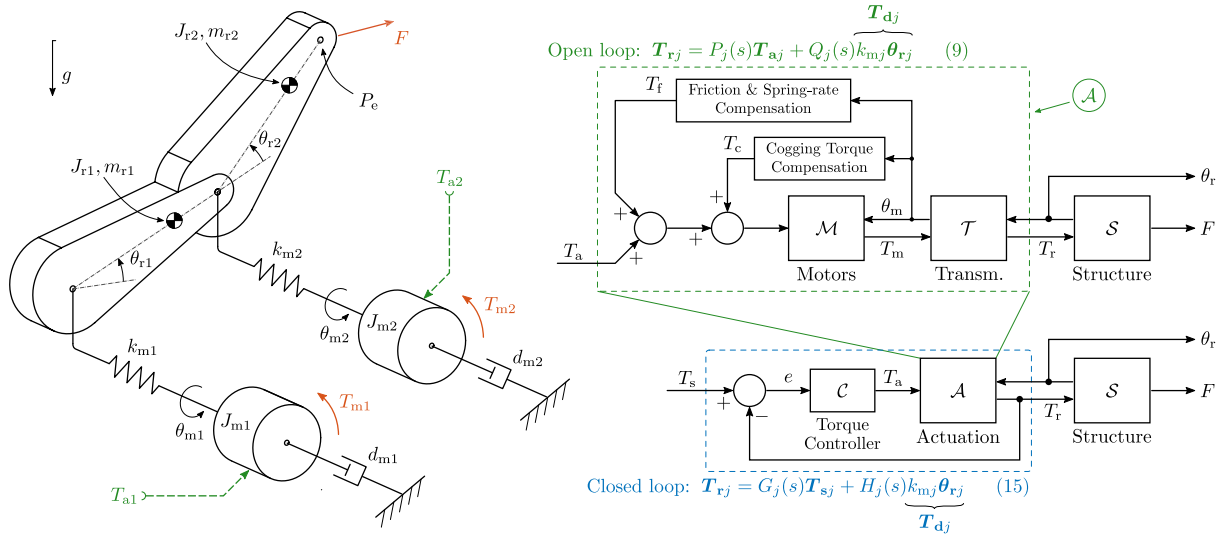
This article has been accepted for inclusion in a future issue of this journal. Content is final as presented, with the exception of pagination.

BOLIGNARI et al.: LIGHTWEIGHT HUMAN-FRIENDLY ROBOTIC ARM BASED ON TRANSPARENT HYDROSTATIC TRANSMISSIONS 5

Fig. 2. Dynamical model of the system and its low-level control scheme. *Left:* Model of the robotic arm according to (4). *Right:* Block-diagram representation of the open-loop precompensated actuators (in green) and the closed-loop low-level torque-control actuators (in blue). The schemes highlight the equation of the torque $T_{\mathrm{r}j}$ delivered to the robot joints in the open-loop (green) and closed-loop (blue) configurations. Notice that this picture is intended to be a reference scheme for equations and text of Sections II–IV. Please refer to these sections for a full understanding of all the shown variables.

open-loop configuration enhances simplicity but lacks the capability of rejecting disturbances, an explicit compensation of the disturbances affecting the motor and the transmission lines assume a relevant role in our work.

A first precompensation action of the motor-transmission units, namely, blocks $\mathcal{M}$ and $\mathcal{T}$, is shown in the green block $\mathcal{A}$ of Fig. 2 (right), comprising the following.

1) The motor cogging torque compensation term $T_{\mathrm{c}} = [T_{\mathrm{c}1}(\theta_{\mathrm{m}1}), T_{\mathrm{c}2}(\theta_{\mathrm{m}2})]^{\top}$, which is in the form of a lookup table emerging from the off-line tuning experiments, reported in [10] and [11], performed on the motors after detaching them from the transmissions' input.

2) The motor-transmission friction and spring-rate compensation term $T_{\mathrm{f}} = [T_{\mathrm{f}1}(\theta_{\mathrm{m}1}, \dot{\theta}_{\mathrm{m}1}), T_{\mathrm{f}2}(\theta_{\mathrm{m}2}, \dot{\theta}_{\mathrm{m}2})]^{\top}$, whose selection for each motor is described next.

Term T_{f} is determined by detaching the robot structure (links) from each motor-transmission subsystem output and performing motor position control following constant-velocity trajectories spanning almost the entire rotation range of the transmission, $\pm 65°$; the velocity is increased at each repetition from 0.1 rad/s to 3 rad/s. The cogging torque compensation term T_{c} is active. The torque input T_{a} required to follow the desired trajectory is shown by the light-grey line in Fig. 3 in the case of the elbow joint. At low speeds, small torque jumps when reversing the rotation direction indicate the presence of Coulomb friction contribution, while the linear trend over constant-velocity strokes highlights some weak linear spring-rate effect introduced by the membranes. At higher velocities viscous quadratic contributions become predominant. This combination of effects is characterized by fitting the following model to the experimental data

$$T_{\mathrm{f}}(\theta_{\mathrm{m}}, \dot{\theta}_{\mathrm{m}}) = T_{\mathrm{v}}(\dot{\theta}_{\mathrm{m}}) + T_{\mathrm{e}}(\theta_{\mathrm{m}}) + T_{\mathrm{u}}(\dot{\theta}_{\mathrm{m}})$$

$$= c_{\mathrm{v}}|\dot{\theta}_{\mathrm{m}}|\dot{\theta}_{\mathrm{m}} + c_{\mathrm{e}}(\theta_{\mathrm{m}} - \theta_0) + c_{\mathrm{u}}\mathbf{sign}(\dot{\theta}_{\mathrm{m}}) \quad (3)$$
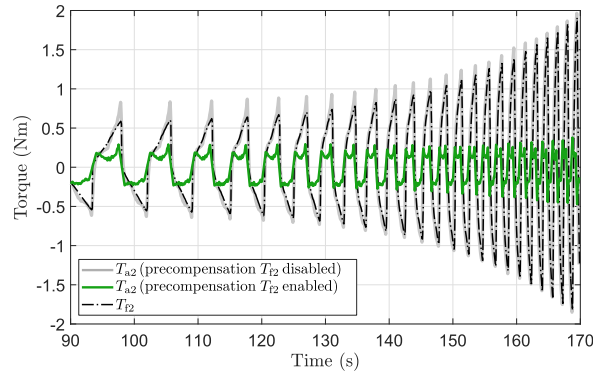

Fig. 3. Characterisation and feed-forward precompensation of the friction and spring-rate effects of the motor-transmission unit, namely blocks $\mathcal{M}$ and $\mathcal{T}$ from Fig. 2. The plotted results are recorded at the elbow joint ($j = 2$); similar results are obtained at the shoulder joint ($j = 1$) since the same, modular, transmission design is used. The motor-transmission unit is position-controlled, following constant-velocity trajectories in the angular range $-65° < \theta_2 < 65°$, while the robot structure $\mathcal{S}$ is detached; the velocity is increased at each repetition. The cogging torque compensation T_{c} is active. The light-grey curve represents the actuation torque $T_{\mathrm{a}2}$ obtained when the precompensation input $T_{\mathrm{f}2}$ is set to zero; the green curve represents $T_{\mathrm{a}2}$ obtained when $T_{\mathrm{f}2}$ is active. The dashed-dotted black curve is the precompensation action $T_{\mathrm{f}2}$ obtained by fitting model (3) to the light-grey experimental data.

where contributions T_{v}, T_{e}, and T_{u} represent the quadratic viscous term, the spring-rate term, and the Coulomb friction term, respectively. Constant $\theta_0 = 0.047$ rad corresponds to the angular position where the intensity of the linear spring-rate effect is zero, while the remaining parameters are calibrated as follows: $c_{\mathrm{v}} = 0.21$ N·m s^2/rad^2, $c_{\mathrm{e}} = 0.28$ N·m/rad and $c_{\mathrm{u}} = 0.28$ N·m. The resulting fit T_{f} is shown by the dashed-dotted black line in Fig. 3. An effective compensation of the friction torque is achieved by adding the feed-forward term T_{f} to the torque reference commanded to the motor driver [see the control scheme in Fig. 2 (right)], as testified by the reduced amplitude of the

green line in Fig. 3, representing the resulting torque command needed to track the same trajectory after applying the friction compensation; the strategy revealed effective especially at high velocities.

B. Precompensated Actuation and Robot Modeling

The left and right pictures in Fig. 2 show a parallel between the physical modeling of the robot and the precompensated block $\mathcal{A}$. The physical system is described by the three main blocks as follows.

1) Block $\mathcal{M}$ contains the dynamics of the motors (it also incorporates the current controller executed by the motor drivers) characterized by moment of inertia $J_{\mathrm{m}j}$ and generating the actuation torques $T_{\mathrm{m}} = [T_{\mathrm{m}1}, T_{\mathrm{m}2}]^\top$.
2) Block $\mathcal{T}$ represents the hydrostatic transmissions in terms of springs, with stiffness $K_{\mathrm{m}} = \mathrm{diag}(k_{\mathrm{m}1}, k_{\mathrm{m}2}) > 0$, and linear dampers, characterized by coefficients $D_{\mathrm{m}} = \mathrm{diag}(d_{\mathrm{m}1}, d_{\mathrm{m}2}) > 0$ which model the residual damping of the transmission (after the precompensation applied in Section III-A) according to an equivalent lumped description.
3) Finally, block $\mathcal{S}$ describes the dynamics of the arm structure, where parameters $m_{\mathrm{r}j}$ and $J_{\mathrm{r}j}$ describe the mass and inertial properties of the links, $P_{\mathrm{e}} = [P_{\mathrm{e}x}, P_{\mathrm{e}y}]^\top$ defines the end-effector position in the workspace, which is a subset of the (x, y) plane, and $F = [F_x, F_y]^\top$ defines the force applied by the robot on the surrounding environment at position P_{e}.

The motors are rigidly connected to the transmission inputs, while the output side of the transmissions are rigidly connected to the links of the arm. These interconnections can be described as force-position feedbacks, where the coupling between $\mathcal{M}$ and $\mathcal{T}$ is described by the motor torques $T_{\mathrm{m}} = [T_{\mathrm{m}1}, T_{\mathrm{m}2}]^\top$ and the motor positions $\theta_{\mathrm{m}} = [\theta_{\mathrm{m}1}, \theta_{\mathrm{m}2}]^\top$, while the coupling between $\mathcal{T}$ and $\mathcal{S}$ is described by the joint torques $T_{\mathrm{r}} = [T_{\mathrm{r}1}, T_{\mathrm{r}2}]^\top$ and the joint positions $\theta_{\mathrm{r}} = [\theta_{\mathrm{r}1}, \theta_{\mathrm{r}2}]^\top$.

After applying the compensation terms T_{c} and T_{f}, described in Section III-A, the equations of motion can be expressed as follows:

$$
\begin{bmatrix} M_{\mathrm{m}} & 0 \\ 0 & M_{\mathrm{r}}(\theta_{\mathrm{r}}) \end{bmatrix} \begin{bmatrix} \ddot{\theta}_{\mathrm{m}} \\ \ddot{\theta}_{\mathrm{r}} \end{bmatrix} + \begin{bmatrix} D_{\mathrm{m}} & 0 \\ 0 & D_{\mathrm{r}} \end{bmatrix} \begin{bmatrix} \dot{\theta}_{\mathrm{m}} \\ \dot{\theta}_{\mathrm{r}} \end{bmatrix}
$$

$$
+ \begin{bmatrix} K_{\mathrm{m}} & -K_{\mathrm{m}} \\ -K_{\mathrm{m}} & K_{\mathrm{m}} \end{bmatrix} \begin{bmatrix} \theta_{\mathrm{m}} \\ \theta_{\mathrm{r}} \end{bmatrix} + \begin{bmatrix} 0 \\ C_{\mathrm{r}}(\theta_{\mathrm{r}}, \dot{\theta}_{\mathrm{r}})\dot{\theta}_{\mathrm{r}} + G_{\mathrm{r}}(\theta_{\mathrm{r}}) \end{bmatrix}
$$

$$
= \begin{bmatrix} I \\ 0 \end{bmatrix} T_{\mathrm{a}} + \begin{bmatrix} 0 \\ J^\top(\theta_{\mathrm{r}}) \end{bmatrix} F \tag{4}
$$

where M_{m} and $M_{\mathrm{r}}(\theta_{\mathrm{r}})$ are the inertia matrices associated with the motors and the robot, respectively, D_{m} and D_{r} are the corresponding damping matrices, and K_{m} is the stiffness matrix associated with the transmissions' stiffness. Matrices $C_{\mathrm{r}}(\theta_{\mathrm{r}}, \dot{\theta}_{\mathrm{r}})\dot{\theta}_{\mathrm{r}}$ and $G_{\mathrm{r}}(\theta_{\mathrm{r}})$ collect the Coriolis and gravity effects, while J is the Jacobian matrix of the robot arm [27]. Subscripts "m" and "r" refer to the motor unit, namely $\mathcal{M}$ and $\mathcal{T}$, and robot structure $\mathcal{S}$, respectively. Variable $T_{\mathrm{a}} = [T_{\mathrm{a}1}, T_{\mathrm{a}2}]^\top$, which collects the

desired joint torques, is the control input of the green block $\mathcal{A}$ in Fig. 2.

C. Analysis and Identification of Torque Dynamics

To suitably represent dynamics (4), we introduce the following change of coordinates (which is always well-defined, since K_{m} is a positive definite matrix):

$$
\begin{bmatrix} T_{\mathrm{r}} \\ \theta_{\mathrm{r}} \end{bmatrix} = \begin{bmatrix} K_{\mathrm{m}} & -K_{\mathrm{m}} \\ 0 & I \end{bmatrix} \begin{bmatrix} \theta_{\mathrm{m}} \\ \theta_{\mathrm{r}} \end{bmatrix} \tag{5}
$$

and, by replacing (5) in (4), we obtain

$$
\begin{bmatrix} M_{\mathrm{m}}K_{\mathrm{m}}^{-1} & M_{\mathrm{m}} \\ 0 & M_{\mathrm{r}}(\theta_{\mathrm{r}}) \end{bmatrix} \begin{bmatrix} \ddot{T}_{\mathrm{r}} \\ \ddot{\theta}_{\mathrm{r}} \end{bmatrix} + \begin{bmatrix} D_{\mathrm{m}}K_{\mathrm{m}}^{-1} & D_{\mathrm{m}} \\ 0 & D_{\mathrm{r}} \end{bmatrix} \begin{bmatrix} \dot{T}_{\mathrm{r}} \\ \dot{\theta}_{\mathrm{r}} \end{bmatrix}
$$

$$
+ \begin{bmatrix} I & 0 \\ -I & 0 \end{bmatrix} \begin{bmatrix} T_{\mathrm{r}} \\ \theta_{\mathrm{r}} \end{bmatrix} + \begin{bmatrix} 0 \\ C_{\mathrm{r}}(\theta_{\mathrm{r}}, \dot{\theta}_{\mathrm{r}})\dot{\theta}_{\mathrm{r}} + G_{\mathrm{r}}(\theta_{\mathrm{r}}) \end{bmatrix}
$$

$$
= \begin{bmatrix} I \\ 0 \end{bmatrix} T_{\mathrm{a}} + \begin{bmatrix} 0 \\ J^\top(\theta_{\mathrm{r}}) \end{bmatrix} F. \tag{6}
$$

In these new coordinates, the transmitted torque T_{r} appears explicitly as a state variable. For each $j = 1, 2$, we may then expand the differential equations governing the state $T_{\mathrm{r}j}$ in scalar form, which gives

$$
\frac{J_{\mathrm{m}j}}{k_{\mathrm{m}j}}\ddot{T}_{\mathrm{r}j} + \frac{d_{\mathrm{m}j}}{k_{\mathrm{m}j}}\dot{T}_{\mathrm{r}j} + T_{\mathrm{r}j} = T_{\mathrm{a}j} - J_{\mathrm{m}j}\ddot{\theta}_{\mathrm{r}j} - d_{\mathrm{m}j}\dot{\theta}_{\mathrm{r}j}. \tag{7}
$$

From the point of view of (7), $T_{\mathrm{a}j}$ is a control input and $T_{\mathrm{r}j}$ is the corresponding system output, while $\theta_{\mathrm{r}j}$ acts as a disturbance on the relationship between $T_{\mathrm{a}j}$ and $T_{\mathrm{r}j}$. This disturbance can be seen as a dynamic effect from the joint angle $\theta_{\mathrm{r}j}$ that is zero with constant angles, and becomes increasingly important as the operation frequency increases. To better quantify the effects of disturbance $\theta_{\mathrm{r}j}$ on the transmitted torque dynamics, we may define a scaled disturbance torque $T_{\mathrm{d}j}$ according to

$$
T_{\mathrm{d}j} = k_{\mathrm{m}j}\theta_{\mathrm{r}j} \tag{8}
$$

so that control input, output, and disturbance are dimensionally equivalent (i.e., they all correspond to torques). By replacing (8) in (7), taking the Laplace transform (bold letters indicate variables in the Laplace domain without indicating explicitly variable "s," i.e., $\boldsymbol{x} := \mathcal{L}[x(t)]$), and solving (7) for variable $\boldsymbol{T_{\mathrm{r}j}}$, we get

$$
\boldsymbol{T_{\mathrm{r}j}} = \frac{\omega_j^2}{s^2 + 2\xi_j\omega_j s + \omega_j^2}\boldsymbol{T_{\mathrm{a}j}} - \frac{s(s + 2\xi_j\omega_j)}{s^2 + 2\xi_j\omega_j s + \omega_j^2}\boldsymbol{T_{\mathrm{d}j}}
$$

$$
= P_j(s)\boldsymbol{T_{\mathrm{a}j}} + Q_j(s)\boldsymbol{T_{\mathrm{d}j}} \tag{9}
$$

where $\omega_j^2 = k_{\mathrm{m}j}/J_{\mathrm{m}j}$ and $\xi_j = c_{\mathrm{m}j}/(2J_{\mathrm{m}j}\omega_j)$ represent the natural frequency and the modal damping of the second-order transfer function $P_j(s)$ from $\boldsymbol{T_{\mathrm{a}j}}$ to $\boldsymbol{T_{\mathrm{r}j}}$, and transfer function $Q_j(s)$ describes the dynamic effect of disturbance $T_{\mathrm{d}j}$. We refer to (9), depicted in green in Fig. 2 (right), as the *open-loop* response, since it describes the system behavior when no torque feedback is applied. Fig. 4 (top) shows the experimental identification of
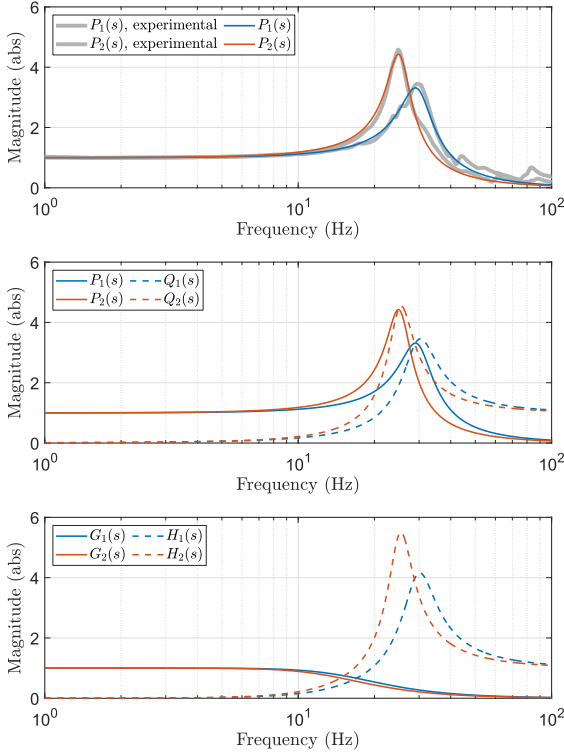
This article has been accepted for inclusion in a future issue of this journal. Content is final as presented, with the exception of pagination.

BOLIGNARI et al.: LIGHTWEIGHT HUMAN-FRIENDLY ROBOTIC ARM BASED ON TRANSPARENT HYDROSTATIC TRANSMISSIONS 7

Fig. 4. Response of shoulder and elbow transmissions in the frequency domain. *Top:* Experimental identification of the open-loop transfer functions $P_j(s)$ in (9). The experimental data are produced by fixing the end-effector to the ground and commanding T_{aj} in the form of chirp functions. The identified dynamical parameters in (9) correspond to $\xi_1 = 0.15$, $\omega_1 = 29.7$ Hz, $\xi_2 = 0.11$ and $\omega_2 = 25.2$ Hz. *Center:* Analytical analysis of the open-loop transfer functions $P_j(s)$ and $Q_j(s)$. *Bottom:* Analytical analysis of the closed-loop transfer functions $G_j(s)$ and $H_j(s)$ described by (15), corresponding to the following selection of the free design parameters in (14): $\xi_{t1} = \sqrt{2}/2$, $\omega_{t1} = 16$ Hz, $\xi_{t2} = \sqrt{2}/2$, and $\omega_{t2} = 14$ Hz (imposing $G_j(s)$ critically damped).

transfer function $P_j(s)$, and Fig. 4 (center) shows the comparison between $P_j(s)$ and $Q_j(s)$ in the frequency domain for both of the hydrostatic transmissions of the 2-DoF manipulator. By replacing $s = \jmath\omega$ in (9) and evaluating the low-frequency limit case, we obtain

$$\boldsymbol{T}_{\mathbf{r}j} \approx \boldsymbol{T}_{\mathbf{a}j} - \jmath\left(2\xi_j \frac{\omega}{\omega_j}\right)\boldsymbol{T}_{\mathbf{d}j}. \qquad (10)$$

Equation (10) reveals that the transmitted torque T_{rj} closely follows T_{aj} as long as the robot operates at relatively low frequencies with respect to the open-loop natural frequency ω_j. The dynamic disturbances T_{dj}, caused by the coupling between the motor and the structure, become nonnegligible as the driving speed increases.

D. Low-Level Closed-Loop Torque Controller

Since in practice the open-loop values of ξ_j and ω_j may lead to unsatisfactory under-damped dynamic performance, we are interested in further improving the open-loop response (9) by closing the low-level feedback control loop in the blue block of Fig. 2 (right). To this end, we exploit the measurements of the joint torques T_{rj} provided by the pressure sensors discussed in Section II. We show below that the transfer function from T_{sj}

(setpoint) to T_{rj} (joint torque) can be arbitrarily shaped by the designer. Afterward, we investigate the influence of disturbance T_{dj} of (8) on this closed-loop architecture.

The closed-loop torque controller $\mathcal{C}$ is decentralized

$$\mathcal{C}(s) = \begin{bmatrix} C_1(s) & 0 \\ 0 & C_2(s) \end{bmatrix} \qquad (11)$$

in order to act separately on each transmission line as follows:

$$\boldsymbol{T}_{\mathbf{a}j} = C_j(s)\boldsymbol{e}_j = C_j(s)\left(\boldsymbol{T}_{\mathbf{s}j} - \boldsymbol{T}_{\mathbf{r}j}\right), \ j = 1, 2. \qquad (12)$$

The structure of $P_j(s)$ in (9) suggests to choose $C_j(s)$ in the form of filtered PIDs with arbitrary time constants τ_{dj} [11]

$$C(s) = k_{pj} + \frac{k_{ij}}{s} + \frac{k_{dj}s}{\tau_{dj}s + 1} = \frac{\bar{k}_{dj}s^2 + \bar{k}_{pj}s + \bar{k}_{ij}}{s\left(\tau_{dj}s + 1\right)} \qquad (13)$$

where k_{pj}, k_{ij}, and k_{dj} are the proportional, integral, and derivative gains of the adopted PID law, while $\bar{k}_{dj} = k_{dj} + k_{pj}\tau_{dj}$, $\bar{k}_{pj} = k_{pj} + k_{ij}\tau_{dj}$ and $\bar{k}_{ij} = k_{ij}$. The controller coefficients are then chosen by arbitrarily fixing the tunable "target" design parameters ξ_{tj} and ω_{tj} to assign the modal damping and natural frequency of the closed loop by selecting

$$\bar{k}_{pj} = \frac{\xi_j\omega_{tj}}{\xi_{tj}\omega_j}, \bar{k}_{ij} = \frac{\omega_{tj}}{2\xi_{tj}}, \bar{k}_{dj} = \frac{\omega_{tj}}{2\xi_{tj}\omega_j^2}, \tau_{dj} = \frac{1}{2\xi_{tj}\omega_{tj}}. \quad (14)$$

In fact, by replacing (12)–(14) in (9), we obtain the desired closed-loop transfer function

$$\boldsymbol{T}_{\mathbf{r}j} = \frac{\omega_{tj}^2}{s^2 + 2\xi_{tj}\omega_{tj}s + \omega_{tj}^2}\boldsymbol{T}_{\mathbf{s}j}$$
$$- \frac{s^2(s + 2\xi_j\omega_j)(s + 2\xi_{tj}\omega_{tj})}{(s^2 + 2\xi_j\omega_j s + \omega_j^2)(s^2 + 2\xi_{tj}\omega_{tj}s + \omega_{tj}^2)}\boldsymbol{T}_{\mathbf{d}j}$$
$$= G_j(s)\boldsymbol{T}_{\mathbf{s}j} + H_j(s)\boldsymbol{T}_{\mathbf{d}j} \qquad (15)$$

showing that the proposed controller successfully replaces the second-order open-loop dynamics $P_j(s)$, described by coefficients ω_j and ξ_j, with the target second-order closed-loop dynamics $G_j(s)$ corresponding to coefficients ω_{tj} and ξ_{tj} freely specified by the designer. The effect of the disturbance $\boldsymbol{T}_{\mathbf{d}j}$ is described by the transfer function $H_j(s)$. We refer to (15) as *closed loop* since it describes the system response when the low-level torque feedback in the blue block in Fig. 2 (right) is applied. The effects of the closed loop and our selection of parameters ω_{tj} and ξ_{tj} are represented in Fig. 4 (bottom) in the frequency domain, showing that the resonance peak of $P_j(s)$ is completely attenuated in $G_j(s)$, while maintaining the torque bandwidth larger than 10 Hz. By considering again the low-frequency limit case of (15), we obtain

$$\boldsymbol{T}_{\mathbf{r}j} \approx \boldsymbol{T}_{\mathbf{s}j} + \left(2\xi_j \frac{\omega}{\omega_j}\right)\left(2\xi_{tj}\frac{\omega}{\omega_{tj}}\right)\boldsymbol{T}_{\mathbf{d}j}. \qquad (16)$$

The comparison between (10) and (16) shows that the low-frequency disturbance effect produced by the joint rotation can be further attenuated with respect to the open-loop case by increasing the closed-loop bandwidth ω_{tj}; this can be visualized in the parametric analysis of $H_j(s)$ in Fig. 5. From (14), we see that choosing a larger ω_{tj} results in higher control
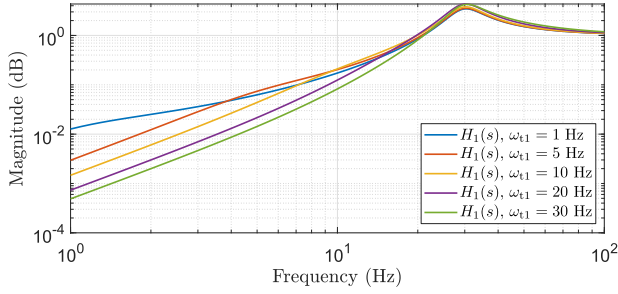
Fig. 5. Parametric analysis of transfer function $H_1(s)$ in (15) with different choices of parameter ω_{t1}. Parameter ξ_{t1} is always selected as $\sqrt{2}/2$ to achieve a critically damped response. The (identified) plant parameters are $\xi_1 = 0.15$, $\omega_1 = 29.7$ Hz. The analysis of joint 2 would show the same trends and is not represented in the picture.

Fig. 6. High-level pHRI controller for active compliance (stiffness and damping) assignment in the operational space. Refer to Fig. 2 (right) for a detailed description of block $\mathcal{R}$.

gains. In practice, the control gains cannot be chosen arbitrarily large due to robustness requirements (e.g., due to the effect of neglected high-frequency dynamics). To further investigate the low-frequency analysis of the proposed scheme, note that (15) implies that T_{rj} tightly follows T_{sj} as long as $G_j(j\omega)$ approaches the unit value and the magnitude of $H_j(j\omega)$ is small, namely

$$|G_j(j\omega)| > 0.95 \quad \text{and} \quad |H_j(j\omega)| < 0.05. \tag{17}$$

Transfer functions $G_j(s)$ and $H_j(s)$ are represented in Fig. 4 (bottom) for experimental values of the model parameters and control gains, showing that the dynamic decoupling (17) holds in the range 0–6 Hz. In this range, the arm $\mathcal{S}$ can be actually controlled by neglecting the motor/transmission dynamics because $T_{rj} \approx T_{sj}$. When this approximation holds true, the differential equation for θ_r appearing in (6) can be approximated as

$$M_r(\theta_r)\ddot{\theta}_r + D_r\dot{\theta}_r + C_r(\theta_r, \dot{\theta}_r)\dot{\theta}_r + G_r(\theta_r) = T_s + J^\top(\theta_r)F \tag{18}$$

where it is clear that T_s plays the same role as the generalized joint torque in conventional robot control schemes, and thus, it can be used to directly control the robot motion/interaction behavior. Notice that the frequency range in which the robot can be effectively force-controlled with stability guarantees goes far beyond the limits set by (17); the robot just starts progressively losing accuracy beyond that limit, because of the decreasing magnitude of $G_j(s)$ and the increasing magnitude of $H_j(s)$.

IV. HIGH-LEVEL pHRI CONTROLLER

The low-level control action developed in Section III is here nested in a high-level feedback loop using the setpoint input T_s to modulate the virtual stiffness and damping response of the robot in the operational space. The overall scheme shapes the human–robot interaction at the end-effector power port $F - \dot{P}_e$. To this end, we consider the robot dynamics with pressure feedback loops, where the low-level controllers have been tuned such that (18) holds true. The high-level controller, represented in Fig. 6, operates by assigning the setpoint input T_s to the block $\mathcal{R}$, implementing the low-level scheme developed in the previous section. Setpoint T_s is selected as an operational space PD with
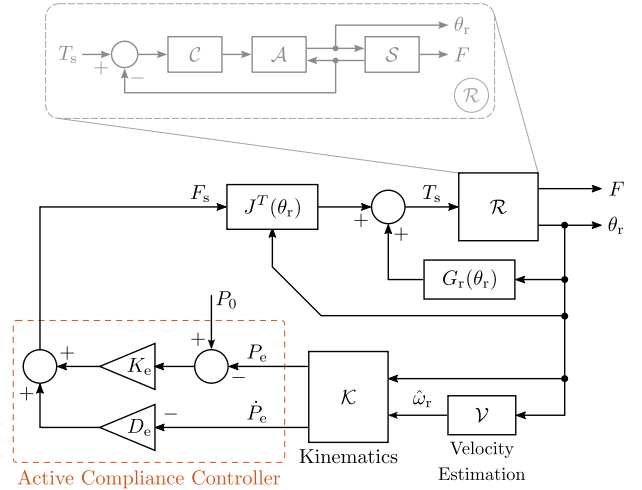
gravity compensation

$$T_s = G_r(\theta_r) - J^\top(\theta_r)F_s$$

$$\text{with } F_s = K_e(P_e(\theta_r) - P_0) + D_e J(\theta_r)\dot{\theta}_r \tag{19}$$

where K_e and D_e are free design parameters corresponding to the virtual stiffness and damping matrices in the operational space, given by

$$K_e = \begin{bmatrix} k_{ex} & 0 \\ 0 & k_{ey} \end{bmatrix} > 0, \quad D_e = \begin{bmatrix} d_{ex} & 0 \\ 0 & d_{ey} \end{bmatrix} > 0 \tag{20}$$

while $P_0 = [P_{0x}, P_{0y}]^\top$ defines the contact-free virtual equilibrium position of the end-effector in the operational space. The actual end-effector position $P_e(\theta_r)$ is computed from the direct kinematics $\mathcal{K}$, while the joint speeds $\dot{\theta}_r$ are estimated through the measurement of θ_r by using high-pass filters, i.e.,

$$\mathcal{V} = \begin{bmatrix} v_1(s) & 0 \\ 0 & v_2(s) \end{bmatrix}, \quad v_j(s) = \frac{k_{fj}s}{s + k_{fj}} \tag{21}$$

where parameters k_{fj} define the filter cutoff frequencies (experimental settings: $k_{f1} = k_{f2} = 50$).

By replacing (19) into (18), the high-level closed-loop dynamics yields

$$M_r(\theta_r)\ddot{\theta}_r + D_r\dot{\theta}_r + J^\top(\theta_r)D_e J(\theta_r)\dot{\theta}_r + C_r(\theta_r, \dot{\theta}_r)\dot{\theta}_r$$

$$+ J^\top(\theta_r)K_e(P_e(\theta_r) - P_0) = J^\top(\theta_r)F. \tag{22}$$

It is observed that, in stationary conditions, (22) implies

$$J^\top(\theta_r)K_e(P_e(\theta_r) - P_0) = J^\top(\theta_r)F \tag{23}$$

and, whenever we are in a nonsingular configuration (i.e., $J(\theta_r)$ is full rank), we get

$$K_e(P_e(\theta_r) - P_0) = F \tag{24}$$

which represents a linear elastic characteristics in the operational space. Quantities K_e and P_0 can then be interpreted as a
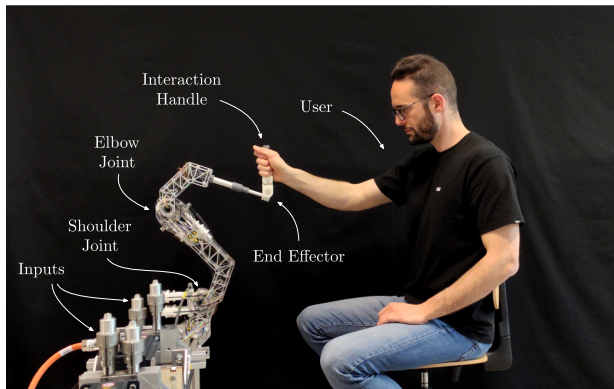
Fig. 7. Experimental setup for human–robot-interaction experiments (notice that the robot base is rotated by 90° in the photo in order to offer a clearer view of the setup, but all the tests are performed in the nominal configuration represented in Fig. 1). Please also see the videos attached as supplementary material.

virtual stiffness and a contact-free end-effector position in the operational space, respectively.

An attractive feature of control law (19) is that it makes the closed-loop system (22) passive at the end-effector port $F - \dot{P}_e$, see [28, Ch. 6]. This can be proven by considering the storage function

$$H(\theta_r, \dot{\theta}_r) = \frac{1}{2}\dot{\theta}_r^\top M_r(\theta_r)\dot{\theta}_r + \frac{1}{2}(P(\theta_r) - P_0)^\top K_e (P(\theta_r) - P_0).$$

$$(25)$$

Differentiating (25) along dynamics (22), and recalling the skew-symmetry of matrix $\dot{M}_r(\theta_r) - 2C_r(\theta_r, \dot{\theta}_r)$, see [27, Ch. 7]), we obtain

$$\dot{H} = -\dot{\theta}_r^\top D_r \dot{\theta}_r - \dot{\theta}_r^\top J^\top(\theta_r) D_e J(\theta_r)\dot{\theta}_r + \dot{\theta}_r^\top J^\top(\theta_r)F$$

$$= -\dot{\theta}_r^\top D_r \dot{\theta}_r - \dot{P}_e^\top D_e \dot{P}_e + \dot{P}_e^\top F$$

$$\leq \dot{P}_e^\top F \qquad (26)$$

which is indeed the well-known passivity inequality. The above discussed passivity property implies that the robot remains stable whenever its end-effector interacts with an external passive system, as long as K_e and D_e are chosen according to (20), [29]. This stability condition includes the interaction with whatever kind of surrounding environment or a human operator, as the human body and limbs are reasonably assumed to show passive dynamics in practical cases, as stated in [30] and remarked in other recent works [31], [32]. The developed architecture is therefore particularly suitable for safe interaction control with unstructured environments. In addition, the second line in (26) shows that D_e permits to directly assign the damping in the operational space.

V. EXPERIMENTS

The proposed mechanical and control design approach is here demonstrated experimentally in pHRI tasks, where the human user sits in front of the robot, at a distance of about 0.5 m from its base, and interacts with the robot's end-effector handle, Fig. 7. The experiments are carried out both in open-loop configuration (9) and in the pressure-feedback closed-loop configuration (15),

to show the intrinsic mechanical response and to highlight the contribution of the proposed controller. The experiments have been conceived to demonstrate the vast potential of hydrostatic transmissions for pHRI in real-world applications. The experiments include easily reproducible tests, similar to those performed in the existing research, e.g., [33] and [34], to simplify the comparison. Specifically, four types of experiments are considered. First, the force-control performance is assessed in Fig. 8 in terms of sinusoidal force tracking experiments. Secondly, actively compensated transparency of the backdrive motion is analyzed in Fig. 9, laying the foundations for the future implementation of enhanced programming-by-demonstration strategies. These strategies should allow operators with no programming experience to quickly and intuitively setup industrial tasks. In a third scenario, backdrivability tests are implemented with an additional payload of 1.5 kg in Fig. 10, thus, showing the effectiveness of RDHT-based robots in collaborative manipulation contexts. Finally, the capability of displaying virtual compliance in the operational space is demonstrated in Fig. 11, which is relevant when developing accurate rehabilitation and teleoperation robots.

A. Sine Tracking Without High-Level pHRI Controller

Force-tracking features in pHRI conditions are assessed by asking the human operator to keep his arm straight and reasonably rigid to hold the handle in a fixed position at the center of the robot workspace. In this configuration, the active-compliance controller is disabled and the outer loop in Fig. 6 is opened, assigning the desired operational-space force F_s in (19) as

$$F_s = \begin{bmatrix} 0 \\ A \sin(2\pi f t) \end{bmatrix} \qquad (27)$$

where constant A is the setpoint amplitude and constant f is the setpoint frequency. The tracking results are shown in Fig. 8. A low-amplitude ($A = 2$ N) and low-frequency ($f = 0.25$ Hz) test is reported in the left plot, which compares the measurement of the F_y component of the force output F produced in open-loop (green line) and closed-loop (blue line) configurations, described by equations (9) and (15), respectively. The tracking error has an average value of 1 N with a maximum value of 1.6 N in open loop, and it is reduced more than three times in closed loop (ave. 0.16 N, max. 0.46 N). This improvement is clearly due to the compensation of the residual bias affecting the output (possibly caused by imperfections in the rolling diaphragms), but is also provided by a closer match with the setpoint (dashed-dotted black line). Similar conclusions can be drawn when repeating the test with a larger setpoint frequency $f = 3$ Hz in Fig. 8 (center), and with a larger setpoint amplitude $A = 10$ N in Fig. 8 (right), testifying that the accuracy of the robot is preserved for faster dynamics and higher forces. Additionally, the interaction force F_{py} computed from the pressure sensor measurements is reported by the purple lines in Fig. 8. These measurements closely match the setpoint and well represent the actual output force F_y measured by the external load cell sensor (notice that the load cell is not involved in the feedback action but it is only used as a ground truth measurement for validation purposes).
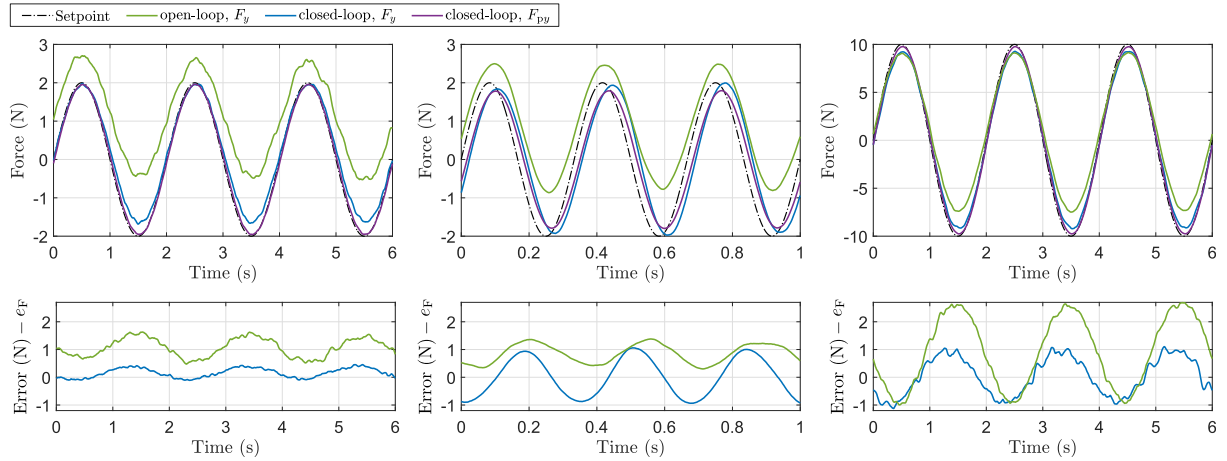
Fig. 8.   Sine tracking experiment. The human user holds the handle at a fixed position and a sinusoidal force reference (dashed-dotted black line) is tracked at the end effector along the y-direction. The green line and the blue line represent the load cell measurement in the open-loop and closed-loop configurations, respectively. The purple line represents the output force measured by means of the pressure sensors in the closed-loop case. *Left:* Low-amplitude low-frequency test ($A = 2$ N, $\omega = 0.25$ Hz); *Center:* Increased setpoint frequency ($A = 2$ N, $\omega = 3$ Hz); *Right:* Increased setpoint amplitude ($A = 10$ N, $\omega = 0.25$ Hz).
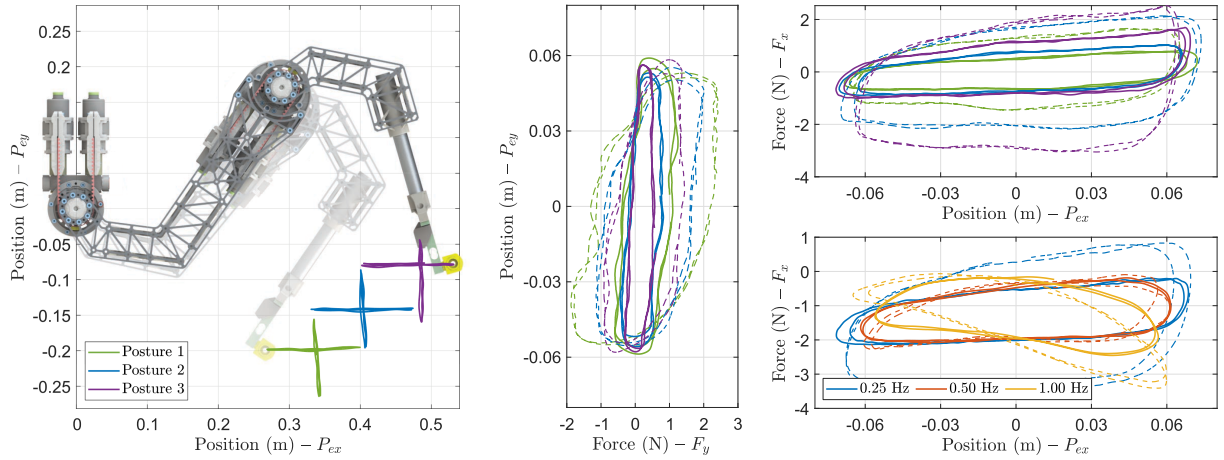

Fig. 9.   Active backdrivability test. F_s is set to zero, while the user imposes a displacement at the end-effector (150 mm amplitude and 0.25 Hz frequency) along the x- and y-directions. Different colors refer to different nominal postures of the robot, while different line styles refer to the control configuration (solid lines for the closed loop, dashed lines for the open loop). *Left:* Vertical and horizontal trajectories performed about three different reference postures. *Center:* Force F_y measured during the vertical displacements. *Top-right:* Force F_x measured during the horizontal displacements. *Bottom-right:* The horizontal test about posture 2 is repeated with different frequencies.
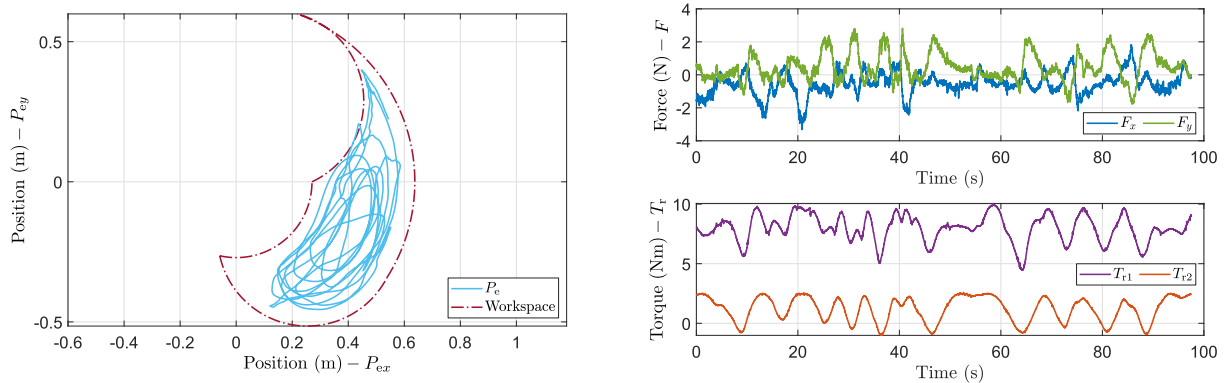

Fig. 10.   Active backdrivability test with an additional 1.5 kg payload fixed close to the end-effector. *Left:* Trajectory imposed at the end-effector by the user (light-blue line) covering a large portion of the reachable workspace (dashed-dotted red line). *Top-right:* End-effector force components F_x and F_y measured by the load-cell. *Bottom-right:* Torque profiles of the shoulder and elbow joints.

This article has been accepted for inclusion in a future issue of this journal. Content is final as presented, with the exception of pagination.

BOLIGNARI et al.: LIGHTWEIGHT HUMAN-FRIENDLY ROBOTIC ARM BASED ON TRANSPARENT HYDROSTATIC TRANSMISSIONS 11
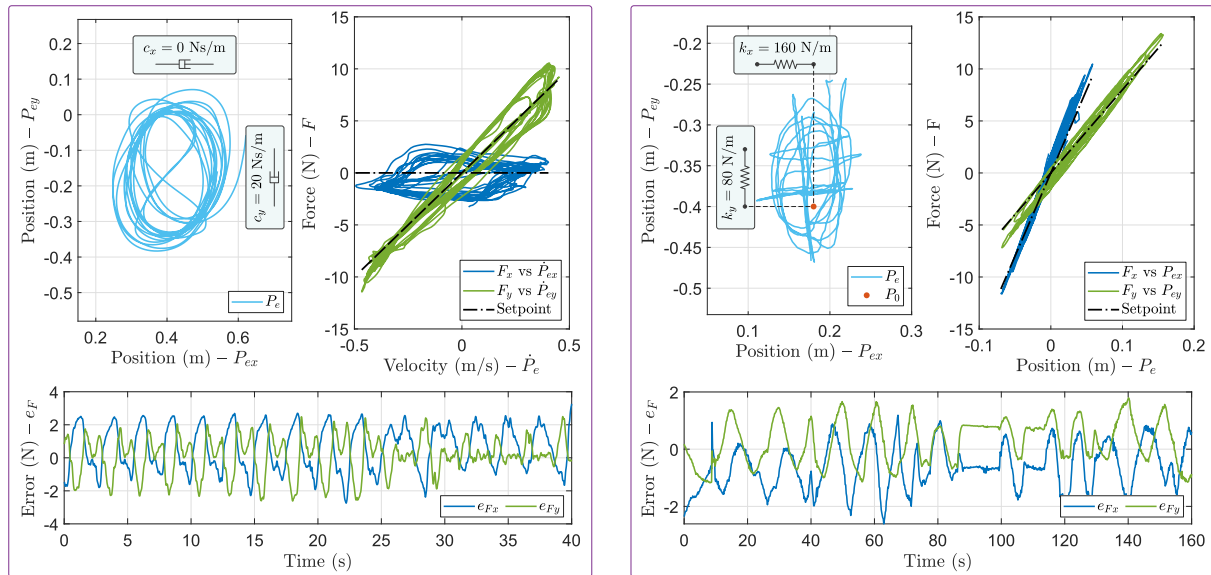

Fig. 11. Experimental assessment of the high-level compliance controller of Fig. 6. The user imposes arbitrary trajectories at the end-effector (light blue lines) while the robot opposes to the motion of the user hand by applying (*Left*) an artificial viscous action and (*Right*) an artificial elastic reaction [the red dot indicates the virtual equilibrium position P_0 in (19)]. Different damping/stiffness coefficients are chosen for the x- and y-axes: $d_{ex} = 0$ Ns/m and $d_{ey} = 20$ Ns/m in the first test, while of $k_{ex} = 160$ N/m and $k_{ey} = 80$ N/m in the second test. In both plots, the *top-left* picture shows the interaction handle position; the *top-right* picture plots the components of both the force reference F_s (black lines) and the actual interaction force F (colored lines) with respect to the corresponding displacement/velocity component; the *bottom* picture show the components of the force tracking error $e_F = F_s - F$.

B. Active Backdrivability Without High-Level pHRI Controller

The response of the robot is further investigated by means of active backdrivability tests that, differently from previous experiments, take into account large displacements. The reference force F_s in (19) is set to zero by selecting the virtual damping $D_e = 0$ and virtual stiffness $K_e = 0$ in the high-level active compliance controller (19). The operator is instructed to keep his arm straight and normally relaxed while moving the end-effector in the vertical and horizontal directions in an oscillatory motion with an amplitude of approximately 150 mm, Fig. 9 (left). Different starting points have been selected to assess the accuracy/transparency of the robot in different workspace areas and directions. Fig. 9 (center) and Fig. 9 (top-right) show the load-cell output measurement $F = [F_x, F_y]^\top$ during low-velocity displacements along the y- and x-directions, respectively: in each plot, colors are used to associate the force measurement with the corresponding trajectory shown in the left picture, while the line style is used to distinguish between the open-loop [dashed lines, system (9)] and closed-loop [solid lines, system (15)] responses. The mean value was subtracted from each position measurement in the force-displacement plots, in order to overlap plots that are actually located in different positions of the workspace, as shown in Fig. 9 (left). The effect of the low-level controller is again clearly visible in these tests, where the closed loop is significantly more accurate and transparent than the open loop. The force required to backdrive the robot attains a peak value of 3.0 N and a standard deviation of 2.2 N in open loop, while a peak value of 1.7 N and a standard deviation of 1.0 N are measured in closed loop (worst-case values); the measurements performed in the closed-loop configuration are

more repeatable. Also, notice how the output is influenced by the posture of the robot: the highest accuracy is obtained with the vertical displacements (y-direction, central plot) when the arm is extended (purple posture), while, the highest accuracy is obtained with the horizontal displacements (x-direction, top-right plot) when the arm is contracted (green posture). In this second case, the purple measurement actually corresponds to the worst performance. This confirms that a planar arm that is fully extended loses control in the direction that runs from the end-effector to the shoulder but controllability is gradually restored in this direction as the elbow joint starts to bend.

Finally, Fig. 9 (bottom-right) shows the force applied by the user while repeating the previous tests about posture 2 at different displacement frequencies, ranging from 0.25 to 1 Hz. In this experimental conditions, there is no clear correlation between velocity and the maximum effort required for the user to backdrive the robot. In addition, the closed-loop measurements appears once again more repeatable that the open-loop ones. This set of high-speed tests (characterized by an end-effector maximum velocity of 0.42 m/s and an elbow-joint maximum velocity of 1.64 rd/s) probably highlights the most relevant difference between the proposed robotic architecture and a traditional industrial/collaborative highly-geared robot, where the former is capable of easily preserving accuracy and transparency features at high velocities. Moreover the measured levels of transparency, both in open loop and closed loop, are also comparable to those achieved by high-performance direct-drive parallel robots [34], but without suffering from workspace limitations, or by cable-driven manipulators, such as kinesthetic haptic devices [35], but without the burden and costs of complex cable transmission systems. The attached video "V1-backdrive" provides an idea of

This article has been accepted for inclusion in a future issue of this journal. Content is final as presented, with the exception of pagination.

12

IEEE TRANSACTIONS ON ROBOTICS

the high level of backdrivability that can be achieved, showing smooth following of the movements of the operator.

A further active-backdrivability test is shown in Fig. 10, where a payload of 1.5 kg is applied in the proximity of the end effector and its weight is suitably taken into account in the control law by an appropriate gravity compensation term. The user, who is again sitting in front of the robot with a normally relaxed arm, imposes a generic motion of the end effector covering almost the entire extension of the reachable workspace, as shown in Fig. 10 (left). The interaction force $F = [F_x, F_y]^\top$, measured at the user hand and shown in Fig. 10 (top-right), remains within the expected limit values measured in the previous free-drive backdrivability experiments, never requiring the user to apply larger forces than 3 N to backdrive the robot. The response is reasonably transparent and uniform over the entire workspace even when the transmission is heavily loaded: in particular, Fig. 10 (bottom-right) shows the torque profile of the two joints recorded during the experiment, revealing an average working torque of about 8 N·m at the shoulder joint, reaching peak values of 10 N·m.

These tests demonstrate a further unique feature of the proposed architecture: in a conventional robotic system, including a high quality cable driven manipulator, friction forces are generally increasing (in most cases proportionally) with the applied forces, leading to a strong dependence on the load of the backdrivability quality. Regarding this, the proposed RDHT manipulator presents a high transparency level, weakly dependent on the programmed applied force. This unique feature may enable the development of new robotic applications where programming by demonstration is smoothly achieved during collaborative tasks that involve load carrying.

C. Testing the High-Level pHRI Controller

The last set of experiments is devoted to evaluating the pHRI performance of the overall control architecture described by Fig. 6 and (19). The robot is here required to display virtual compliance in the operational space, against the displacements imposed by the human operator, by introducing viscous or elastic forces along certain artificial programmed directions. Two sets of experiments are performed, the first one in Fig. 11 (left) with pure damping assignment [$K_e = 0$ in (19)] and the second one in Fig. 11 (right) with pure stiffness assignment [$D_e = 0$ in (19)]. K_e and D_e are selected diagonal in (19) and different damping/stiffness coefficients are specified along the x- and y-axes, in order to challenge the robot to exhibit sufficiently rich compliance actions. $K_e = 0$ N/m and $D_e = \mathrm{diag}(0, 20)$ Ns/m are selected for the damping experiment, while $K_e = \mathrm{diag}(160, 80)$ N/m and $D_e = 0$ Ns/m are selected for the stiffness experiments. Both tests show similar tracking errors (bottom plots of Fig. 11) along the x- and y-axes, highlighting a desirably uniform force tracking accuracy over a range of different load intensities along the two axes. These results also testify to a good decoupling of the force controllability along the two axes. Consistently with the results of Fig. 9, a maximum error of 2.7 N is measured in the first test, and a maximum error of 2.5 N is measured in the second one. Such an ability to accurately produce artificial mechanical impedance demonstrates that the proposed RDHT could be employed to develop novel robots for rehabilitation and haptics applications. A similar application is exemplified in the attached video "V2-haptic."

VI. CONCLUSION

In this article, we presented a novel 2-DoF robotic arm that featured grounded electrical actuators and RDHTs: an architecture that intrinsically provided accurate torque transmission alongside with a large bandwidth and a simple/low-cost implementation. Through an accurate dynamic characterization of the designed arm, we introduced and studied a hierarchical controller solely based on the feedback from low-cost pressure sensors (without expensive load cells or force sensors).

The experiments demonstrated accurate stable closed-loop force setpoint control with arm-transmission dynamics decoupling up to 6 Hz and structural resonance attenuation. Moreover, the proposed manipulator and control system had been further tested in pHRI tasks, showing smooth closed-loop controlled backdrivability that was comparable to that of haptic devices, which usually relied on complex and expensive cable-based transmission systems. Furthermore, we demonstrated a unique feature of RDHT-based robotic systems: the ability to maintain a high level of backdrivability even while compensating for external loads. Finally, high levels of accuracy had been achieved in human–robot interaction tasks that involved displaying virtual stiffness and damping.

The experimental results suggested that the proposed technology was a good candidate to develop a new generation of human-friendly robots, such as co-bots or humanoids, leveraging on structural simplicity, unconditional safety, and improved accuracy of the interaction and manipulation tasks. The enhanced active backdrivability illustrated in Section V-B was suitable for implementing human–robot collaboration and improved programming-by-demonstration approaches. These properties, together with the capability of accurately generating virtual compliance responses in the operational space (shown in Section V-C), also suggested the promising use of hydrostatic transmissions in developing innovative, cost-effective, and accurate rehabilitation exoskeletons, as well as force-controllable leader and follower arms in teleoperated robotic systems.

Future developments will address the following challenges: 1) design and implementation of a 6-DoF manipulator, finding effective solutions for the routing scheme of the large number of hoses that must be introduced along the robotic structure and that need to bend smoothly during the manipulator motion; 2) improvement of the structural performance through the optimization of the stiffness of the structural components and through the minimization of the mass and inertia; 3) characterization of the long-term cyclical fatigue response of the RHDT joint, with the implementation of specific long-duration experimental campaigns; 4) introduction of programmable physical damping, through the employment of electric control valves within the hydraulic circuits.

This article has been accepted for inclusion in a future issue of this journal. Content is final as presented, with the exception of pagination.

BOLIGNARI et al.: LIGHTWEIGHT HUMAN-FRIENDLY ROBOTIC ARM BASED ON TRANSPARENT HYDROSTATIC TRANSMISSIONS

13

REFERENCES

[1] A. De Santis, B. Siciliano, A. De Luca, and A. Bicchi, "An atlas of physical human–robot interaction," *Mechanism Mach. Theory*, vol. 43, no. 3, pp. 253–270, 2008.

[2] G. Hirzinger, A. Albu-Schaffer, M. Hahnle, I. Schaefer, and N. Sporer, "On a new generation of torque controlled light-weight robots," in *Proc. Int. Conf. Robot. Autom.*, 2001, pp. 3356–3363.

[3] G. A. Pratt and M. M. Williamson, "Series elastic actuators," in *Proc. IEEE/RSJ Int. Conf. Intell. Robots Syst.*, 1995, pp. 399–406.

[4] B. Vanderborght et al., "Variable impedance actuators: A review," *Robot. Auton. Syst.*, vol. 61, no. 12, pp. 1601–1614, 2013.

[5] K. Salisbury, W. Townsend, B. Ebrman, and D. DiPietro, "Preliminary design of a whole-arm manipulation system (WAMS)," in *Proc. Int. Conf. Robot. Autom.*, 1988, pp. 254–260.

[6] A. Frisoli, F. Salsedo, M. Bergamasco, B. Rossi, and M. C. Carboncini, "A force-feedback exoskeleton for upper-limb rehabilitation in virtual reality," *Appl. Bionics Biomech.*, vol. 6, no. 2, pp. 115–126, 2009.

[7] S. Grosu et al., "Driving robotic exoskeletons using cable-based transmissions: A qualitative analysis and overview," *Appl. Mechanics Rev.*, vol. 70, no. 6, 2018, Art. no. 060801.

[8] Y.-J. Kim, "Design of low inertia manipulator with high stiffness and strength using tension amplifying mechanisms," in *Proc. IEEE/RSJ Int. Conf. Intell. Robots Syst.*, 2015, pp. 5850–5856.

[9] J. P. Whitney, M. F. Glisson, E. L. Brockmeyer, and J. K. Hodgins, "A low-friction passive fluid transmission and fluid-tendon soft actuator," in *Proc. IEEE/RSJ Int. Conf. Intell. Robots Syst.*, 2014, pp. 2801–2808.

[10] M. Bolignari and M. Fontana, "Design and experimental characterization of a high performance hydrostatic transmission for robot actuation," *Meccanica*, vol. 55, no. 5, pp. 1169–1179, 2020.

[11] M. Bolignari, G. Rizzello, L. Zaccarian, and M. Fontana, "Smith-predictor-based torque control of a rolling diaphragm hydrostatic transmission," *IEEE Robot. Autom. Lett.*, vol. 6, no. 2, pp. 2970–2977, Apr. 2021.

[12] J. P. Whitney, T. Chen, J. Mars, and J. K. Hodgins, "A hybrid hydrostatic transmission and human-safe haptic telepresence robot," in *Proc. Int. Conf. On Robot. Autom.*, 2016, pp. 690–695.

[13] S. Frishman, R. D. Ings, V. Sheth, B. L. Daniel, and M. R. Cutkosky, "Extending reach inside the MRI bore: A 7-DOF, low-friction, hydrostatic teleoperator," *IEEE Trans. Med. Robot. Bionics*, vol. 3, no. 3, pp. 701–713, Aug. 2021.

[14] S. Frishman, A. Kight, I. Pirozzi, M. C. Coffey, B. L. Daniel, and M. R. Cutkosky, "Enabling in-bore MRI-guided biopsies with force feedback," *IEEE Trans. Haptics*, vol. 13, no. 1, pp. 159–166, Jan.–Mar. 2020.

[15] Z. Dong et al., "High-performance continuous hydraulic motor for MR safe robotic teleoperation," *IEEE Robot. Autom. Lett.*, vol. 4, no. 2, pp. 1964–1971, Apr. 2019.

[16] N. Burkhard et al., "A rolling-diaphragm hydrostatic transmission for remote MR-guided needle insertion," in *Proc. Int. Conf. Robot. Autom.*, 2017, pp. 1148–1153.

[17] M. Bolignari, G. Moretti, and M. Fontana, "Design and experimental characterisation of a hydrostatic transmission for upper limb exoskeletons," in *Proc. IEEE/RSJ Int. Conf. Intell. Robots Syst.*, 2018, pp. 2768–2773.

[18] C. Khazoom, C. Véronneau, J.-P. L. Bigué, J. Grenier, A. Girard, and J.-S. Plante, "Design and control of a multifunctional ankle exoskeleton powered by magnetorheological actuators to assist walking, jumping, and landing," *IEEE Robot. Autom. Lett.*, vol. 4, no. 3, pp. 3083–3090, Jul. 2019.

[19] C. Véronneau, J.-P. L. Bigué, A. Lussier-Desbiens, and J.-S. Plante, "A high-bandwidth back-drivable hydrostatic power distribution system for exoskeletons based on magnetorheological clutches," *IEEE Robot. Autom. Lett.*, vol. 3, no. 3, pp. 2592–2599, Jul. 2018.

[20] C. Véronneau et al., "Multifunctional remotely actuated 3-DOF supernumerary robotic ARM based on magnetorheological clutches and hydrostatic transmission lines," *IEEE Robot. Autom. Lett.*, vol. 5, no. 2, pp. 2546–2553, Apr. 2020.

[21] C. Véronneau, J. Denis, L.-P. Lebel, M. Denninger, J.-S. Plante, and A. Girard, "A lightweight force-controllable wearable ARM based on magnetorheological-hydrostatic actuators," in *Proc. Int. Conf. Robot. Autom.*, 2019, pp. 4018–4024.

[22] C. Khazoom, P. Caillouette, A. Girard, and J.-S. Plante, "A supernumerary robotic leg powered by magnetorheological actuators to assist human locomotion," *IEEE Robot. Autom. Lett.*, vol. 5, no. 4, pp. 5143–5150, Oct. 2020.

[23] E. Schwarm, K. M. Gravesmill, and J. P. Whitney, "A floating-piston hydrostatic linear actuator and remote-direct-drive 2-DOF gripper," in *Proc. Int. Conf. Robot. Autom.*, 2019, pp. 7562–7568.

[24] M. Bolignari, A. Mo, M. Fontana, and A. Badri-Spröwitz, "Diaphragm ankle actuation for efficient series elastic legged robot hopping," in *Proc. IEEE/RSJ Int. Conf. Intell. Robots Syst.*, 2022, pp. 4279–4286.

[25] C. Wang and J. P. Whitney, "Series elastic force control for soft robotic fluid actuators," 2020, *arXiv:2004.01269*.

[26] J. Denis, J.-S. Plante, and A. Girard, "Low-level force-control of MR-hydrostatic actuators," *IEEE Robot. Autom. Lett.*, vol. 6, no. 2, pp. 3849–3856, Apr. 2021.

[27] B. Siciliano, L. Sciavicco, L. Villani, and G. Oriolo, *Robot.: Modelling, Plan. , Control*, Berlin, Germany: Springer-Verlag, 2010.

[28] H. K. Khalil, *Nonlinear Systems*. Richardson, TX, USA: Patience Hall, vol. 115, 2002.

[29] N. Hogan and S. P. Buerger, "Impedance and interaction control," in *Robotics and Automation Handbook*. Boca Raton, FL, USA: CRC, 2018, pp. 375–398.

[30] N. Hogan, "Controlling Impedance At the man/machine Interface," in *Proc. IEEE Int. Conf. Robot. Autom.*, 1989, pp. 1626–1627.

[31] A. Haddadi, K. Razi, and K. Hashtrudi-Zaad, "Operator dynamics consideration for less conservative coupled stability condition in bilateral teleoperation," *IEEE/ASME Trans. Mechatron.*, vol. 20, no. 5, pp. 2463–2475, Oct. 2015.

[32] A. Q. Keemink, H. van der Kooij, and A. H. Stienen, "Admittance control for physical human–robot interaction," *Int. J. Robot. Res.*, vol. 37, no. 11, pp. 1421–1444, 2018.

[33] B. Kim and A. D. Deshpande, "An upper-body rehabilitation exoskeleton harmony with an anatomical shoulder mechanism: Design, modeling, control, and performance evaluation," *J. Robot. Res.*, vol. 36, no. 4, pp. 414–435, 2017.

[34] K. Wen, T. S. Nguyen, D. Harton, T. Laliberté, and C. Gosselin, "A back-drivable kinematically redundant (6+3)-degree-of-freedom hybrid parallel robot for intuitive sensorless physical human–robot interaction," *IEEE Trans. Robot.*, vol. 37, no. 4, pp. 1222–1238, Aug. 2021.

[35] F. Gosselin and A. Riwan, "Design of VIRTUOSE 3D: A new haptic interface for teleoperation and virtual reality," in *Proc. Int. Conf. Adv. Robot.*, 2001, pp. 205–212.

Marco Bolignari received the Ph.D. degree in mechatronics engineering from the University of Trento, Trento, Italy, in 2022.

In 2021, he was a Visiting Researcher with the Dynamic Locomotion Group, Max Planck Institute for Intelligent Systems. In 2022, he joined Scuola Superiore Sant'Anna, Pisa, Italy, as a Postdoc Researcher. His main research interest includes the development of innovative mechanisms for industrial and medical robots.

Gianluca Rizzello (Member, IEEE) received the Ph.D. degree in information and communication technologies from Scuola Interpolitecnica di Dottorato, Turin, Italy, in 2016.

He joined the Saarland University, Saarbrücken, Germany, as the Group Leader of Smart Material Modeling and Control from 2016 to 2019, and since 2020 he has been an Assistant Professor of Adaptive Polymer Systems. His research interests include modeling and control of innovative mechatronic and robotic systems based on smart materials and structures.

Luca Zaccarian (Fellow, IEEE) received the Ph.D. degree in computer and control engineering from the University of Roma Tor Vergata, Rome, Italy, in 2000.

Since 2011, he has been the Directeur de Recherche with LAAS-CNRS, Toulouse, France. Since 2013, he has been a Professor with the University of Trento, Trento, Italy. His main research interests include the analysis and design of nonlinear and hybrid control systems.

Dr. Zaccarian was the recipient of the O. Hugo Schuck Best Paper Award by the American Automatic Control Council in 2001.

Marco Fontana received the Ph.D. degree in robotics from Scuola Superiore Sant'Anna, Pisa, Italy, in 2008.

Since 2020, he has been an Associate Professor in Mechanical Engineering with Scuola Superiore Sant'Anna. His main research interests include the development and optimization of innovative hardware solutions for advanced robots, mechatronic systems, and energy harvesters.